IOPscience iopscience.iop.org

Home Search Collections Journals About Contact us My IOPscience

Scalar calibration of vector magnetometers

This content has been downloaded from IOPscience. Please scroll down to see the full text.

2000 Meas. Sci. Technol. 11 120

(http://iopscience.iop.org/0957-0233/11/2/304)

View the table of contents for this issue, or go to the journal homepage for more

Download details:

IP Address: 93.180.53.211
This content was downloaded on 04/02/2014 at 09:09

Please note that terms and conditions apply.

Meas. Sci. Technol. **11** (2000) 120–132. Printed in the UK PII: S0957-0233(00)05824-0

Scalar calibration of vector magnetometers

J M G Merayo, P Brauer, F Primdahl†, J R Petersen† and O V Nielsen

Department of Automation, Technical University of Denmark, Building 327, 2800 Lyngby, Denmark

E-mail: jmgm@iau.dtu.dk

Received 7 July 1999, in final form and accepted for publication 5 November 1999

Abstract. The calibration parameters of a vector magnetometer are estimated only by the use of a scalar reference magnetometer. The method presented in this paper differs from those previously reported in its linearized parametrization. This allows the determination of three offsets or signals in the absence of a magnetic field, three scale factors for normalization of the axes and three non-orthogonality angles which build up an orthogonal system intrinsically in the sensor. The advantage of this method compared with others lies in its linear least squares estimator, which finds independently and uniquely the parameters for a given data set. Therefore, a magnetometer may be characterized inexpensively in the Earth's magnetic-field environment. This procedure has been used successfully in the pre-flight calibration of the state-of-the-art magnetometers on board the magnetic mapping satellites Ørsted, Astrid-2, CHAMP and SAC-C. By using this method, full-Earth-field-range magnetometers (±65536.0 nT) can be characterized down to an absolute precision of 0.5 nT, non-orthogonality of only 2 arcsec and a resolution of 0.2 nT.

Keywords: calibration, tri-axial magnetometer, least squares, linearization

1. Introduction

A calibration must be performed prior to the use of an instrument. It should be based on a realistic model that will cover reliably all the fields to which the instrument will be exposed in the measuring survey. Once the parameters which describe the behaviour of the output referred to the sensed quantity have been found, the relationship between the engineering units (analogue-to-digital converter outputs) and the physical units is known. It is also necessary to express their temperature dependences, long-term drifts and any other possible change dependent on other physical quantities.

Almost every spacecraft has been flown with a magnetometer whose application is scientific and/or for implementing attitude manoeuvres. Sometimes the satellite carries two of them, which may be used for gradient measurements of magnetic natural signatures, for compensation of satellite-body disturbances or for in-flight calibration, if one of the magnetometers is an absolute scalar magnetometer. The POGO series in the 1960s included some of the first magnetically oriented missions, in which global magnetic maps were derived solely from measurements of the intensity of the field. It was soon discovered that these maps derived from scalar data only lack accuracy for some of the spherical harmonic terms, often called the *Backus effect* (see Backus 1970). The effect is enhanced by the fact that the magnetic signal at the spacecraft altitude is not completely derivable from a potential function; furthermore, the curl of B does not vanish. This is due to, among other sources, ionospheric currents, which are stronger in the auroral zones, and to the equatorial electro-jet currents. In 1979–80 the 7-month mission MAGSAT was designed to carry out a vector magnetic mapping, with a 1 nT resolution tri-axial flux-gate magnetometer. The instrument had a very sophisticated arrangement for the sensor to be located several metres away from the body and advanced electronics for that time in order to get the accuracy of 17 bits. This type of instrument is now widely used for space applications because it is inexpensive, power saving, light and measures the magnetic field in one range. As a counterpart to this, its absolute and pointing accuracy depends on other instrumentation (i.e. a scalar magnetometer and a star imager) such that their combination sets the ultimate absolute accuracy.

A scalar proton magnetometer is widely used for calibration, since it provides a direct measurement of the intensity of the magnetic field B in an absolute sense. Once the specimen in the sensor has been polarized in the presence of an external field B, the excited protons precess at a frequency proportional to that field B. This relation is dependent only on universal constants. This kind of instrument has typically 0.02 nT resolution and 0.1 nT precision. However, precautions should be taken since the sensor has a range between 60 and 20 μT and a maximum field of view of $\pm 60^\circ$ in the direction of B.

† Also at the Danish Space Research Institute, Juliane Maries vej, 2100 København Ø, Denmark.

0957-0233/00/020120+13$30.00 © 2000 IOP Publishing Ltd

A star imager establishes the relation between the magnetic reference system of the magnetometer and an absolute inertial system, in which the magnetic elements are provided. The magnetometer pointing accuracy is approximately 1 arcsec, which imposes a demand for very high resolution onto the star imager as well as requiring mechanical stability of the optical bench on which both instruments are sitting. The scope of this paper is, nevertheless, limited to analysing the intrinsic parameters of a magnetometer before they can be related to an absolute system. A forthcoming paper will describe how to find this relationship between the star imager and the vector magnetometer.

In general, the magnetic field measured by a magnetometer can be written as a function of its three output quantities, Q_i, in an arbitrary coordinate system defined by the unit vectors $\boldsymbol{u}_i$:

$$\boldsymbol{B} = \mathbf{A}_0^i \cdot \boldsymbol{u}_i + \mathbf{A}_1^{ij} Q_i \cdot \boldsymbol{u}_j + \mathbf{A}_2^{ijk} Q_i Q_j \cdot \boldsymbol{u}_k + \mathbf{A}_3^{ijkl} Q_i Q_j Q_k \cdot \boldsymbol{u}_i + \cdots \quad (1)$$

where the tensors $\mathbf{A}_0$, $\mathbf{A}_1$, $\mathbf{A}_2$, $\mathbf{A}_3$, ... denote the offset, linear, second-order, third-order and higher order terms, respectively, and summation follows tensor notation. An understanding of the construction and behaviour of the sensor gives us the knowledge for a more concise, simplified and at the same time complete model. For example in Brauer *et al* (1997), the transverse effect appears only in the plane of the ring-core sensor due to there being an uncompensated field in the direction transverse to the measurement.

Other calibrating procedures have customarily been devised to obtain the coefficients of the magnetometer. As illustrated by Primdahl (1986), this can be done by rotating the sensor around three axes and so finding the relation between two axes perpendicular to the third axis. In other cases, a vector coil system has been used to determine these parameters. Earlier mathematical methods using the scalar field as a reference had been developed, but these have non-linear iterative solutions, which may lead to problems with convergence, uniqueness and stability (see Langel 1994 and Neubert 1995).

The method presented in this paper takes advantage of the linearization of the scalar field as a function of the measured components of a vector magnetometer that avoids the need for non-linear iteration. Initially, the sensors and their intrinsic reference systems are described. The parametrization and estimator which are used to determine the solution to the problem are presented. Following this, a comparison with a non-linear model is drawn and a discussion about how the quality of the solution depends on various factors is presented. Small disturbances may be added to the model in order to describe non-linearities, temperature dependences and long term drift effects.

2. The CSC and CDC magnetic sensors

The Space Magnetometer Group at IAU-DTU (`http://www.iau.dtu.dk/csc/`) has developed the magnetometers on board the magnetic mapping satellites Ørsted, Astrid-2, CHAMP and SAC-C. They all carry a compact spherical coil (CSC) sensor except for Astrid-2, which has

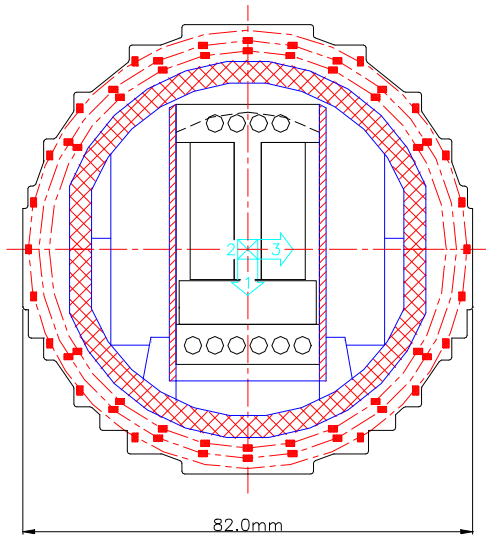

Figure 1. The CSC flux-gate sensor for the magnetometers on board the Ørsted, SAC-C and CHAMP satellites.

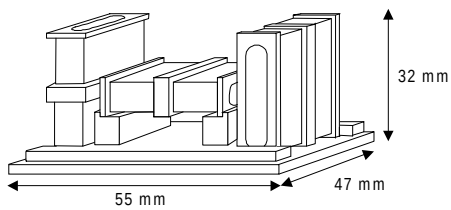

Figure 2. The CDC flux-gate sensor for the magnetometer on board the Astrid-2 satellite.

a compact detector coil (CDC) instead. The types of magnetic instrumentation on Ørsted and Astrid-2 are described in papers by Nielsen *et al* (1995) and Brauer *et al* (1998), respectively.

Although the latter has a digital feed-back loop instead of the traditional analogue electronics circuitry, the principle of operation of the flux-gate sensor is similar in both cases. Therefore, a single function will characterize totally any electronic channel. This function, which is temperature dependent and may be linear, contains the offset and the scale factor as the only set of parameters necessary to describe the outputs of the instrument. These are usually measured in the laboratory. If the digital output of the analogue-to-digital converter, N_i (24 bits in the case of Ørsted and 20 bits for Astrid-2), is normalized to match the full-scale range $\pm 65\,536$ and if the instrument-field-range design aim is $\pm 65\,536.0$ nT, then the engineering units related to a temperature reference, ΔT, may be written as follows:

$$EU_i = a_{i0}(\Delta T) + a_{i1}(\Delta T) N_i + a_{i2}(\Delta T)\left(\frac{N_i}{2^{16}}\right)^2 + a_{i3}(\Delta T)\left(\frac{N_i}{2^{16}}\right)^3 \ldots . \quad (2)$$

In the latter equation, the coefficients a_{ij} are all represented in the same units (eu), except for a_{i1}, which will be nearly unity. This gives the convenience of being able to compare the ratios among them by use of the naked

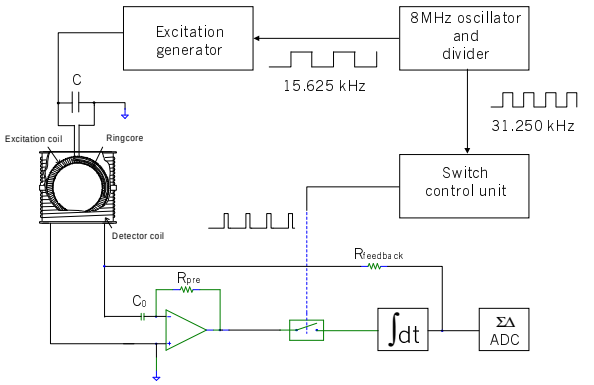

Figure 3. The flux-gate electronics block diagram (excitation and one channel). The output is connected to a $\Sigma\Delta$ analogue-to-digital converter of 24 bits.

eye, assuming, for example, positive or negative full range, which makes the terms in brackets ± 1. Therefore, a_{i2} and a_{i3} directly give the deviation from linearity for full range.

The CSC, depicted in figure 1, was designed by Primdahl and Jensen (1982) in such a way that the feedback compensation of the field to the flux-gate transducers is carried out in a vectorially homogeneous way. This means that a pure nulled vector field is created in the sensor volume, with the external field subtracted from the homogeneous compensation field. Therefore, the tri-axial flux-gate elements are used as zero-field detectors, so the response of the CSC is linear. Furthermore, the material which supports the compensating coils and which determines the pointing and absolute accuracy of the CSC is chosen to provide a very good thermal stability, see Nielsen *et al* (1997).

The CDC sensor, displayed in figure 2 and described by Brauer *et al* (1997), is single-axis compensated and made from ring-core sensors. The geometry is similar to the one in the MAGSAT mission, although it is scaled down in size and volume, and the core material is amorphous metal. This configuration lacks the possibility of creating a homogeneous null field in the sensor, allowing an uncompensated field to exist transverse to the direction of detection of each sensor. This seems to be the cause of non-linearities when the field in the transverse direction in the plane of the ring-core is large and not compensated.

The mechanical construction of the sensor support is machined out by very accurate milling tools, which can resolve 0.1 mm. The CSC, with a radius of approximately 4.5 cm, is made from two symmetrical half spheres, which are attached to a turning pivot in order to machine the grooves which will contain the copper wire. Therefore, the maximum error one could expect between the machining plane and the rotating axis is less than 10 arcmin. The scale factor of any of the axes is proportional to the inverse of its radius, which gives rise to a relative error of less than 0.25%, depending also on the thickness of the copper wire. The CDC suffers from the same limitations, but when all three sensors are glued together onto the support, the angular relation between them can be worse, say by a factor of five, than that for the CSC. All this means that the mechanical axes are not far from being orthogonal and the scale factors will be close to the design values.

The electronics contributes to the sensitivity as well as to the offset. The precision feedback resistor combined with the coil constant sets the overall gain and it can be off by up to 1%. Figure 3 is a block diagram of the electronics of the excitation and one channel for the flux-gate sensor. The offset comes mainly from two sources: firstly, the 60–70 dB attenuation of the feedthrough signal in the synchronous phase detector that can be equivalent to up to 1000 nT; and secondly, the bias current of the integrator amplifier, which can rise to an offset of a few nanoteslas.

The noise of the sensor is about 15 pT_{RMS}, but the resolution of the ADC sets the limit on the dynamic range of the instrument, which is 21.5 bits effectively, equivalent to 130 dB. Hence, the calibration process should be able to resolve the nine parameters with this accuracy. A typical flux-gate sensor output is plotted in figure 4, in which a square wave of amplitude 1 nT has been applied. The noise may be appreciated as the ripple on the output signal.

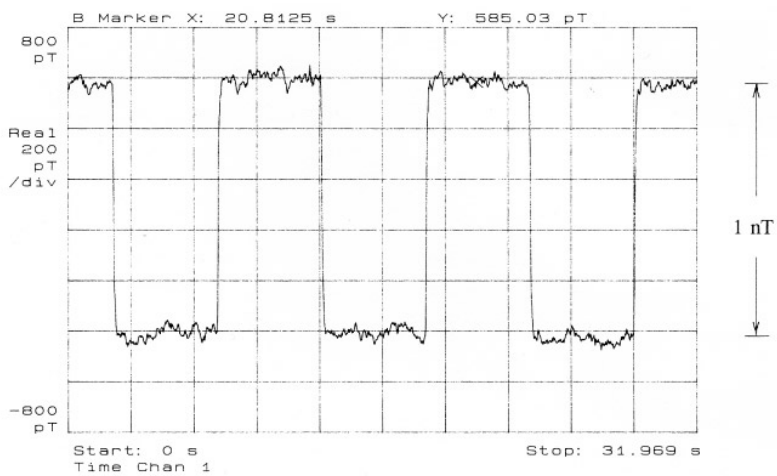

Figure 4. The flux-gate output on applying a square-wave signal on amplitude 1 nT.

As we will see, the magnetic tri-axial sensor can provide by itself a very accurate reference frame without any reference to an external coordinate system. In order to establish the relation between these two systems, some kinds of assumptions and definitions must be made. The next section describes how to build up an orthogonal system in the sensor, which must be done in order to establish a base for all observations.

3. The intrinsic reference-frame system in tri-axial sensors

Any vector can be expressed as a linear combination of an independent set of vectors, which constitute a basis for that specific space; consequently for the three-dimensional space:

$$\boldsymbol{B} = \alpha_1 \boldsymbol{u}_1 + \alpha_2 \boldsymbol{u}_2 + \alpha_3 \boldsymbol{u}_3 = \beta_1 \boldsymbol{w}_1 + \beta_2 \boldsymbol{w}_2 + \beta_3 \boldsymbol{w}_3 \quad (3)$$

where $\{\alpha_1, \alpha_2, \alpha_3\}$ and $\{\beta_1, \beta_2, \beta_3\}$ are the components of the vector in the orthonormal basis $\{\boldsymbol{u}_1, \boldsymbol{u}_2, \boldsymbol{u}_3\}$ and any arbitrary basis, $\{\boldsymbol{w}_1, \boldsymbol{w}_2, \boldsymbol{w}_3\}$, respectively. The latter, which is intrinsic to the sensor, is precisely the system in which the instrument provides the magnetic quantities and it depends only on the mechanical precision of the machining process.

According to this, the intrinsic reference-frame system (IRFS) of a specific sensor is defined in matrix form as follows:

$$\begin{bmatrix} \boldsymbol{u}_1 \\ \boldsymbol{u}_2 \\ \boldsymbol{u}_3 \end{bmatrix} \equiv \mathbf{T} \begin{bmatrix} \boldsymbol{w}_1 \\ \boldsymbol{w}_2 \\ \boldsymbol{w}_3 \end{bmatrix} \equiv \begin{bmatrix} 1 & 0 & 0 \\ \gamma_1 & \gamma_2 & 0 \\ \xi_1 & \xi_2 & \xi_3 \end{bmatrix} \begin{bmatrix} \boldsymbol{w}_1 \\ \boldsymbol{w}_2 \\ \boldsymbol{w}_3 \end{bmatrix}. \quad (4)$$

In other words, the first mechanical axis, $\boldsymbol{w}_1$, is defined to be completely aligned with the first orthonormal axis of the IRFS, $\boldsymbol{u}_1$. The second orthonormal axis, $\boldsymbol{u}_2$, lies in the plane defined by the first and second mechanical axes, $\boldsymbol{w}_1$ and $\boldsymbol{w}_2$, and it is almost aligned to the latter, $\boldsymbol{w}_2$. Customarily the third orthonormal axis, $\boldsymbol{u}_3$, which is nearly aligned with the third mechanical axis, $\boldsymbol{w}_3$, is defined as the cross product of the first and second axes for completion of the base in the right-handed sense in a dextro-giro system. The closer to orthonormal the mechanical basis, the closer the transformation matrix to the identity matrix, or the coefficients γ_2, ξ_3 and γ_1, ξ_1 and ξ_2 to one and zero, respectively. Figure 5 illustrates the IRFS, with the assumption that the non-orthogonal angles ν_{12}, ν_{13} and ν_{23} are very small.

The previous definition can be rewritten in a more convenient way:

$$\boldsymbol{u}_1 \equiv \boldsymbol{w}_1$$

$$\boldsymbol{u}_2 \equiv \boldsymbol{u}_3 \times \boldsymbol{w}_1 = \gamma_1 \boldsymbol{w}_1 + \gamma_2 \boldsymbol{w}_2$$

$$\boldsymbol{u}_3 \equiv \frac{\boldsymbol{w}_1 \times \boldsymbol{w}_2}{|\boldsymbol{w}_1 \times \boldsymbol{w}_2|} = \xi_1 \boldsymbol{w}_1 + \xi_2 \boldsymbol{w}_2 + \xi_3 \boldsymbol{w}_3. \quad (5)$$

Since the basis $\{\boldsymbol{u}_1, \boldsymbol{u}_2, \boldsymbol{u}_3\}$ is orthonormal, $\boldsymbol{u}_i \cdot \boldsymbol{u}_j = \delta_{ij}$, which can be applied to find the angles between the vectors of the basis $\{\boldsymbol{w}_1, \boldsymbol{w}_2, \boldsymbol{w}_3\}$. It should be mentioned, though, that the usual Euclidean norm might be used for the orthonormal basis vectors only. A general algebra describes the vectors in the non-orthogonal basis and this must be taken into account when taking inner and outer products or performing any other

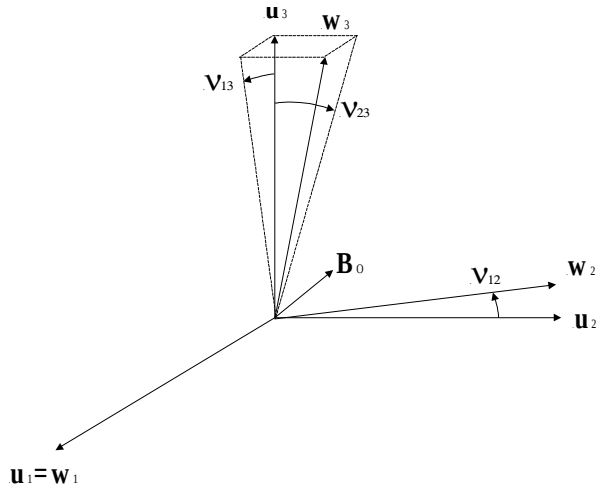

Figure 5. The intrinsic reference-frame system (IRFS) of a sensor is built up from its non-orthogonal mechanical axes.

operation. The rows of the matrix $\mathbf{T}$ are the components of the unitary vectors $\boldsymbol{u}_i$ in the mechanical system. Then, after algebraic manipulation, the following relations are found:

$$\boldsymbol{u}_2 = -\frac{c_{12}}{(1-c_{12}^2)^{1/2}} \boldsymbol{w}_1 + \frac{1}{(1-c_{12}^2)^{1/2}} \boldsymbol{w}_2$$

$$\frac{\boldsymbol{u}_2}{\xi_3} = \frac{c_{12}c_{23} - c_{13}}{1-c_{12}^2} \boldsymbol{w}_1 + \frac{c_{12}c_{13} - c_{23}}{1-c_{12}^2} \boldsymbol{w}_2 + \boldsymbol{w}_3. \quad (6)$$

It is easily seen that the bases are related only by the knowledge of three quantities, which are the angles between the vectors of the non-orthogonal basis as functions of the parameters γ_i and ξ_i. These, c_{ij} $(i \neq j)$, which are defined to be the cosines of the angles between vectors of the mechanical basis, are calculated and their first-order approximations are

$$c_{12} \equiv \cos(\boldsymbol{w}_1, \boldsymbol{w}_2) = -\frac{\gamma_1}{\gamma_2} \cong -\gamma_1$$

$$c_{13} \equiv \cos(\boldsymbol{w}_1, \boldsymbol{w}_3) = -\frac{\xi_1}{\xi_3}(1-c_{12}^2)^{1/2} + c_{12}c_{23} \cong -\frac{\xi_1}{\xi_3} \cong -\xi_1$$

$$c_{23} \equiv \cos(\boldsymbol{w}_2, \boldsymbol{w}_3) = -\frac{\xi_2}{\xi_3}(1-c_{12}^2)^{1/2} + c_{12}c_{13} \cong -\frac{\xi_2}{\xi_3} \cong -\xi_2 \quad (7)$$

where the approximations are valid for small angular deviations between $\boldsymbol{w}_i$ and $\boldsymbol{u}_i$. The parameter ξ_3, which is computed by normalizing the vector $\boldsymbol{u}_3$, is expressed as a function of the quantities c_{ij} thus:

$$\xi_3 = \pm\left(\frac{1-c_{12}^2}{1-c_{12}^2-c_{23}^2-c_{13}^2+2c_{12}c_{23}c_{13}}\right)^{1/2}$$

$$\cong \pm\left(\frac{1-c_{12}^2}{1-c_{12}^2-c_{23}^2-c_{13}^2}\right)^{1/2}. \quad (8)$$

It is observed in some cases that, upon extracting square roots, a phase change of π may occur. In this situation, the sign is to be chosen so that the direction of the resulting vector is, as defined, usually positive if the mechanical basis of the sensor is dextro-giro. An inversion of one of these signs may result in a levo-giro or left-handed system, a situation that is not desirable. This happens to be the case for γ_2 and

ξ_3. In order to avoid truncation in the numerical operations, a special precaution has been taken in the formulae for the quantities c_{12}, c_{13} and c_{23}. All divisions are performed with the parameters γ_2 and ξ_3 in order to avoid the situation of division by a very small number. It is demonstrable that the rows of the matrix in equation (4) constitute the direction vectors, but to operate on them the usual Euclidean norm does not apply, but rather the appropriate norm for the space defined by the skew basis $\{\boldsymbol{w}_1, \boldsymbol{w}_2, \boldsymbol{w}_3\}$.

4. The linearized parameter model

The relation between the non-orthogonal and the orthonormal bases, $\mathbf{T}$, as shown in (4), is linear. Therefore, the components are related also by a linear transformation, which is the inverse of the matrix $\mathbf{T}$ transposed, i.e. $[\mathbf{T}^{-1}]^{\mathrm{T}}$. In the equation (3), $\{\alpha_1, \alpha_2, \alpha_3\}$ represent the physical components of the field in the orthonormal basis and $\{\beta_1, \beta_2, \beta_3\}$ are the measurements in the non-orthogonal basis. The measurements in engineering units, $\{EU_1, EU_2, EU_3\}$ are null-centred by the offset vector $\{O_1, O_2, O_3\}$ and normalized with respect to the physical units (nT) with the positive-defined sensitivities $\{s_1, s_2, s_3\}$. In the CSC sensor, the field compensation is carried out in the vector sense. In contrast, the CDC sensor does individual-component compensations. Thus, for the CSC

$$\alpha_i = B_i \qquad \beta_i = s_i(EU_i - O_i). \tag{9}$$

Therefore, the relation between the physical magnetic field $\boldsymbol{B}$ in the IRFS and the measurements is obtained by combining the last definition and the relation between the quantities $\{\alpha_1, \alpha_2, \alpha_3\}$ and $\{\beta_1, \beta_2, \beta_3\}$, hence

$$\begin{bmatrix} B_1 \\ B_2 \\ B_3 \end{bmatrix}_{IRFS} \equiv [\mathbf{T}^{-1}]^{\mathrm{T}} \begin{bmatrix} s_1(EU_1 - O_1) \\ s_2(EU_2 - O_2) \\ s_3(EU_3 - O_3) \end{bmatrix} \tag{10a}$$

$$= \begin{bmatrix} 1 & -\frac{\gamma_1}{\gamma_2} & \frac{\gamma_1\xi_2 - \gamma_2\xi_1}{\gamma_2\xi_3} \\ 0 & -\frac{1}{\gamma_2} & -\frac{\xi_2}{\gamma_2\xi_3} \\ 0 & 0 & -\frac{1}{\xi_3} \end{bmatrix} \begin{bmatrix} s_1(EU_1 - O_1) \\ s_2(EU_2 - O_2) \\ s_3(EU_3 - O_3) \end{bmatrix} \tag{10b}$$

$$= \mathbf{A} \begin{bmatrix} EU_1 - O_1 \\ EU_2 - O_2 \\ EU_3 - O_3 \end{bmatrix} \tag{10c}$$

where including the sensitivities s_i in the matrix results in the following transformation $\mathbf{A}$:

$$\mathbf{A} \equiv \begin{bmatrix} a_{11} & a_{12} & a_{13} \\ 0 & a_{22} & a_{23} \\ 0 & 0 & a_{33} \end{bmatrix} \tag{11a}$$

$$= \begin{bmatrix} s_1 & -\frac{\gamma_1}{\gamma_2}s_2 & \frac{\gamma_1\xi_2 - \gamma_2\xi_1}{\gamma_2\xi_3}s_3 \\ 0 & \frac{1}{\gamma_2}s_2 & -\frac{\xi_2}{\gamma_2\xi_3}s_3 \\ 0 & 0 & \frac{1}{\xi_3}s_3 \end{bmatrix} \tag{11b}$$

$$\cong \begin{bmatrix} s_1 & -\gamma_1 s_2 & -\xi_1 s_3 \\ 0 & s_2 & -\xi_2 s_3 \\ 0 & 0 & s_3 \end{bmatrix}. \tag{11c}$$

It is clear that the physical magnetic field $\boldsymbol{B}$ may be computed from the instrument readings provided that the set of nine coefficients is known. This set consisting of three offsets, three sensitivities and three non-orthogonal angles entirely describes the magnetometer. According to what has been mentioned above about the upper limit for the coefficients, the matrix $\mathbf{A}$ can be approximated to first order as shown. In any case, the matrix $\mathbf{A}$ and the vector $\boldsymbol{O}$ establish a linear relationship between the calibrated and uncalibrated quantities. This will be the foundation for the estimate of the magnetometer parameters in the following.

The scalar field, which is measured by the reference magnetometer, must be compared with the square root of the sum of squares of the physical components. The dot product is computed and, after manipulating the expression, the following can be found:

$$\begin{aligned} \boldsymbol{B}\cdot\boldsymbol{B} = \boldsymbol{B}_0\cdot\boldsymbol{B}_0 &+ a_{11}^2 EU_1^2 + (a_{12}^2 + a_{22}^2)EU_2^2 \\ &+(a_{13}^2 + a_{23}^2 + a_{33}^2)EU_3^2 + 2a_{11}a_{12}EU_1EU_2 \\ &+2(a_{12}a_{13} + a_{22}a_{23})EU_2EU_3 + 2a_{11}a_{13}EU_3EU_1 \\ &-2(a_{11}^2 O_1 + a_{11}a_{12}O_2 + a_{11}a_{13}O_3)EU_1 - 2[a_{11}a_{12}O_1 \\ &+(a_{12}^2 + a_{22}^2)O_2 + (a_{12}a_{13} + a_{22}a_{23})O_3]EU_2 \\ &-2[a_{11}a_{13}O_1 + (a_{12}a_{13} + a_{22}a_{23})O_2 \\ &+(a_{13}^2 + a_{23}^2 + a_{33}^2)O_3]EU_3 \end{aligned} \tag{12}$$

$$\boldsymbol{B}_0 \equiv \mathbf{A}\begin{bmatrix} O_1 \\ O_2 \\ O_3 \end{bmatrix}. \tag{13}$$

The first term, B_0^2, is the square of the residual field strength due to the sensor offset in nanoteslas. The terms containing the EU_i^2 represent the modulus of the engineering vector in the mechanical basis, since the columns of $\mathbf{A}$ are the components of $\boldsymbol{B}$ in the mechanical basis. The remaining terms are the cross couplings between the components EU_i and their offsets, referred to the orthonormal basis, which is the result of dealing with a non-orthogonal system.

It is observed that, although the computation of the scalar field is a non-linear operation in the components, its square can be expressed as a linear combination of terms EU_iEU_j and EU_i. This fact is used in the parametrization to solve the problem in a least-squares-linear sense. Therefore, the following representation uses the vectorial form:

$$\begin{aligned} B^2 - B_0^2 = [\, &EU_1^2 \quad EU_1 \quad EU_2^2 \quad EU_2 \quad EU_3^2 \quad EU_3 \\ &EU_1EU_2 \quad EU_2EU_3 \quad EU_3EU_1 \,]\cdot\boldsymbol{p} \end{aligned} \tag{14}$$

where the vector $\boldsymbol{p}$ is identified to be

$$\begin{bmatrix} p_1 \\ p_2 \\ p_3 \\ p_4 \\ p_5 \\ p_6 \\ p_7 \\ p_8 \\ p_9 \end{bmatrix} = \begin{bmatrix} a_{11}^2 \\ -2(a_{11}^2 O_1 + a_{11}a_{12}O_2 + a_{11}a_{13}O_3) \\ a_{12}^2 + a_{22}^2 \\ -2[a_{11}a_{12}O_1 + (a_{12}^2 + a_{22}^2)O_2 \\ +(a_{12}a_{13} + a_{22}a_{23})O_3] \\ a_{13}^2 + a_{23}^2 + a_{33}^2 \\ -2[a_{11}a_{13}O_1 + (a_{12}a_{13} + a_{22}a_{23})O_2 \\ +(a_{13}^2 + a_{23}^2 + a_{33}^2)O_3] \\ 2a_{11}a_{12} \\ 2(a_{12}a_{13} + a_{22}a_{23}) \\ 2a_{11}a_{13} \end{bmatrix}. \tag{15}$$

If the vector $\boldsymbol{p}$ is known, it is possible to compute the elements of the matrix $\mathbf{A}$ and the components of the vector $\boldsymbol{O}$. It can easily be done by algebraic manipulation of the expressions in the proper order. Consequently, a_{11} is found from p_1, a_{12} from p_7, a_{13} from p_9, a_{22} from p_3, a_{23} from p_8 and a_{33} from p_3. O_1, O_2 and O_3 are computed by taking into account all parameters. The following formulae show

the relations between them and their expressions as functions of the components of $\boldsymbol{p}$:

$$
\begin{aligned}
a_{11} &\equiv +\sqrt{p_1} \\
a_{12} &= \frac{p_7}{2a_{11}} = \frac{p_7}{2\sqrt{p_1}} \\
a_{13} &= \frac{p_9}{2a_{11}} = \frac{p_9}{2\sqrt{p_1}} \\
a_{22} &\equiv +(p_3 - a_{12}^2)^{1/2} = \left(p_3 - \frac{p_7^2}{4p_1}\right)^{1/2} \\
a_{23} &= \frac{p_8/2 - a_{12}a_{13}}{a_{22}} = \frac{2p_1p_8 - p_7p_9}{2(4p_1^2p_3 - p_1p_7^2)^{1/2}} \\
a_{33} &= \pm(p_5 - a_{13}^2 - a_{23}^2)^{1/2} \\
&= \pm\left[p_5 - \frac{p_9^2}{4p_1} + \left(\frac{2p_1p_8 - p_7p_9}{2(4p_1^2p_3 - p_1p_7^2)^{1/2}}\right)^2\right]^{1/2} \qquad (16)
\end{aligned}
$$

$$
\begin{bmatrix} O_1 \\ O_2 \\ O_3 \end{bmatrix} = \begin{bmatrix} -2p_1 & -p_7 & -p_9 \\ -p_7 & -2p_3 & -p_8 \\ -p_9 & -p_8 & -2p_5 \end{bmatrix}^{-1} \begin{bmatrix} p_2 \\ p_4 \\ p_6 \end{bmatrix}. \qquad (17)
$$

It is interesting to observe, as indicated above, that some freedom in choosing the sign is allowed. In order to be consistent with the IRFS definition, a_{11} and a_{22} are chosen to be positive, which is reflected in the formulae (16) and (17) and, therefore, there is no ambiguity for the signs of a_{12}, a_{13} and a_{23}. In contrast, a_{33} is the parameter that can make the IRFS be dextro-giro (if it is positive) or levo-giro (if it is negative). This can yield a misinterpretation of the angular relations between the unitary vectors if it is not done correctly.

However, it is straightforward to find out whether the sensor system is right- or left-handed, by exposing it to the ambient field in the three approximately axial directions, or by performing full rotations about an arbitrary axis as described by Primdahl *et al* (1999). If the sensor turns out to be right-handed (left-handed), then the sign of a_{33} must be positive (negative). This is, naturally, in accordance with the signs of γ_2 and ξ_3 shown in (5)–(8).

5. The estimation criteria

In order to find the parameter vector $\boldsymbol{p}$, some kind of criterion which will estimate $\boldsymbol{p}$ with sufficient confidence and robustness must be selected. A linear least-squares procedure is the candidate chosen. This minimizes the sum of the square residuals of the objective function and gives the best estimate for the given quality of the data used in the computation process.

Equation (14) can be rewritten in this manner, by using the parameter vector $\boldsymbol{p}$. If N different measurements are assumed to have been taken by rotating the sensor systematically, so that at least the full ranges of the components are sensed (the next section will discuss the procedure used to accomplish this) then equation (14) becomes

$$
\begin{bmatrix} B^2|_1 \\ B^2|_2 \\ B^2|_3 \\ \cdots \\ \cdots \\ \cdots \\ \cdots \\ \cdots \\ \cdots \\ B^2|_{N-1} \\ B^2|_N \end{bmatrix} - \begin{bmatrix} 1 \\ 1 \\ 1 \\ \cdots \\ \cdots \\ \cdots \\ \cdots \\ \cdots \\ \cdots \\ 1 \\ 1 \end{bmatrix} B_0^2 = \begin{bmatrix}
EU_1^2|_1 & EU_1|_1 & EU_2^2|_1 & EU_3|_1 & EU_1EU_2|_1 & EU_2EU_3|_1 & EU_3EU_1|_1 \\
EU_1^2|_2 & EU_1|_2 & EU_2^2|_2 & EU_3|_2 & EU_1EU_2|_2 & EU_2EU_3|_2 & EU_3EU_1|_2 \\
EU_1^2|_3 & \cdot & EU_2^2|_3 & \cdot & \cdot & \cdot & \cdot \\
\cdot & \cdot & \cdot & \cdot & \cdot & \cdot & \cdot \\
\cdot & \cdot & \cdot & \cdot & \cdot & \cdot & \cdot \\
\cdot & \cdot & \cdot & \cdot & \cdot & \cdot & \cdot \\
\cdot & \cdot & \cdot & \cdot & \cdot & \cdot & \cdot \\
\cdot & \cdot & \cdot & \cdot & \cdot & \cdot & \cdot \\
\cdot & \cdot & \cdot & \cdot & \cdot & \cdot & \cdot \\
EU_1^2|_{N-1} & \cdot & EU_2^2|_{N-1} & \cdot & \cdot & \cdot & \cdot \\
EU_1^2|_N & EU_1|_N & EU_2^2|_N & EU_3|_N & EU_1EU_2|_N & EU_2EU_3|_N & EU_3EU_1|_N
\end{bmatrix} \begin{bmatrix} p_1 \\ p_2 \\ p_3 \\ p_4 \\ p_5 \\ p_6 \\ p_7 \\ p_8 \\ p_9 \end{bmatrix} \qquad (18)
$$

or, in matrix form,

$$
\underset{N\times 1}{\mathbf{B}^2} - \underset{N\times 1}{\mathbf{1}}\, B_0^2 = \underset{N\times 9}{\mathbf{D}} \cdot \underset{9\times 1}{\boldsymbol{p}}\,. \qquad (19)
$$

The terms on the left-hand side of (19) are the squared reference scalar fields reduced by the magnetometer's squared residual scalar fields. This obviously represents a problem, since the reference field is decremented by a factor of up to 0.0001%, when the strength of B_0 is of the order of 50 nT in a background of 50 μT, and by 0.01% if B_0 is 500 nT. This influences directly the scale factors, which will be mismatched by the same error. The offsets will also be altered, but their errors can be hidden in their standard deviations if their mean values are sufficiently small. In contrast, the non-orthogonality angles will not be affected by it. Fortunately, this effect may be neglected in some cases.

To overcome this problem, an iterative modified approach may be used. The parameter vector $\boldsymbol{p}$ is then estimated by initially putting $B_0 = 0$ in (19). In the least-squares sense, this is

$$
\begin{aligned}
\underset{9\times 1}{\boldsymbol{p}^*} &= [\ \underset{9\times N}{\mathbf{D}^{\mathrm{T}}}\ \underset{N\times N}{\mathbf{W}}\ \underset{N\times 9}{\mathbf{D}}\ ]^{-1} \\
&\quad \times \underset{9\times N}{\mathbf{D}^{\mathrm{T}}}\ \underset{N\times N}{\mathbf{W}}\ \underset{N\times 1}{\mathbf{B}^2}\,. \qquad (20)
\end{aligned}
$$

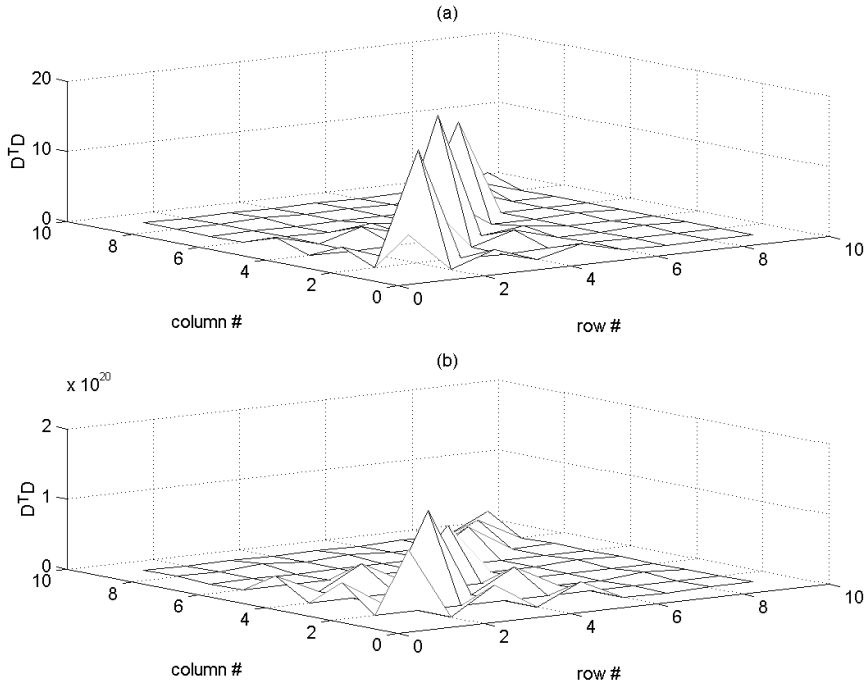

Figure 6. The difference between (*a*) normalizing the covariance matrix $\mathbf{D}^{\mathrm{T}}\mathbf{D}$ by the maximum range (2^{16} nT) and (*b*) the case without any scaling.

At this point, it is assumed that the weighting matrix **W** is the identity matrix. This calculation is executed in a numerical analysis package, for example MATLAB® from The MathWorks Inc.

By observing the matrix **D**, it is evident that the difference between columns will be very large, since numbers of the order of $65\,536^2$ have to be related to numbers close to zero. This requires a very high computing precision, when operations with numbers of 10^{10} and small numbers will be compared. Proper normalization of the EU_i components by the full-range value (usually 2^{16}) will avoid this truncation problem. As a result of this normalization, all elements of the matrix **D** are of the order of unity and hence it will be more economical for computing. Figure 6 shows the difference between values of the matrix $\mathbf{D}^{\mathrm{T}}\mathbf{D}$, after (*a*) and before (*b*) normalization in a linear mesh plot. The *x* and *y* planes show the rows and columns, respectively, and the *z* axis plots the value of the elements of the resulting matrix. The case (*a*) will definitely minimize problems regarding the inversion of such a matrix for the solution of $\boldsymbol{p}$. Once this has been done, the dimensions are restored in $\boldsymbol{p}$, accordingly.

Then the transformation matrix **A** and offset vector $\boldsymbol{O}$ are computed by using (16) and (17), respectively. This serves to evaluate the predicted components of $\boldsymbol{B}$ and the process is repeated to estimate a new matrix and offset vector.

By having the initial conditions of **A** and $\boldsymbol{O}$ being the identity matrix and a zero vector, respectively, $\boldsymbol{B}$ is predicted from the current parameters $\boldsymbol{p}^*_{n-1}$ found in the $(n-1)$th iteration (the initial conditions are for $n = 1$). Hence, $\boldsymbol{B}$ is then used as the input for the algorithm for the nth iteration and a new estimate of the parameter vector $\boldsymbol{p}$ is found, $\boldsymbol{p}^*_n$. This $\boldsymbol{p}^*_n$ provides new estimates of a^*_{ijn} and O^*_{in}, which are used to adjust the parameters. Since a_{ii} are connected to the sensitivities, they will approach unity when n is large enough, provided that the quality of the data is reasonable. Therefore, they are subject to a multiplying correction. In contrast, a_{ij} $(i \neq j)$ and O_i are associated with the non-orthogonal angles and the offsets, respectively. The offset is clearly an additive quantity in the iteration process. This is also the case for the non-orthogonality angles, if it is assumed that the angles are sufficiently small, as indicated in section 2. The fact that these angles are scaled by the sensitivities in the matrix **A** does not affect this, since the iterative sensitivities tend towards unity. The process is schematized by compiling all iterations into the following matrix:

$$\mathbf{A} \cong \mathbf{A}_n \ldots \mathbf{A}_1\mathbf{A}_0 \cong \begin{bmatrix} \prod_{k=0}^{n} s_1^k & -\gamma_1^0 s_2^0 + s_1^0 \sum_{k=1}^{n} \gamma_1^k & -\xi_1^0 s_3^0 + s_1^0 \sum_{k=1}^{n} \xi_1^k \\ 0 & \prod_{k=0}^{n} s_2^k & -\xi_2^0 s_3^0 + s_2^0 \sum_{k=1}^{n} \xi_2^k \\ 0 & 0 & \prod_{k=0}^{n} s_3^k \end{bmatrix}. \tag{21}$$

This first order approximation shows the adjustment of the elements of the matrix **A**. Once the first iteration has been completed, $\mathbf{A}_0$, then the next computation $(k = 1)$ will estimate an almost unity matrix. Nevertheless, the new elements a^k_{ij} are still used to correct the current parameters. This is illustrated in the next expression, which shows the manner in which the parameters are adjusted and their ideally estimated convergence values ($i = 1, 2, 3$ and $j > i$):

$$a_{ii}|_n = a_{ii}|_{n-1}[1 + k_1(a^*_{ii}|_n - 1)] \qquad a^*_{ii}|_n \xrightarrow{n\gg} 1$$

$$a_{ij}|_n = a_{ij}|_{n-1} + k_2 a^*_{ij}|_n \qquad a^*_{ij}|_n \xrightarrow{n\gg} 0$$

$$O_i|_n = O_i|_{n-1} + k_3 O^*_i|_n \qquad O^*_i|_n \xrightarrow{n\gg} 0 \Rightarrow B^{*2}_0|_n \longrightarrow 0. \tag{22}$$

As pointed out in (22), the value which B_0^2 approaches for large n is zero. This solves for the situation in which the reference field suffers a decrement, as indicated above. Consequently, the sensitivities are no longer affected by the residual offset.

The rate of convergence of the parameters is controlled by the factors k_i, which in general are set to unity. Alternatively they can follow a rate established as a function of the iteration number according to

$$k_i = \exp\left(1 - \frac{n}{\tau}\right) \qquad \tau \geqslant n. \tag{23}$$

This serves also to simulate the Gauss method in the non-linear least-squares process, which regulates the speed of the convergence. It also allows simulation of the effect of adjusting the offset, sensitivities and non-orthogonalities independently.

6. The influence of the quality of data on the parameters

Two main sources may influence dramatically the quality of the solution: firstly, the distribution of the data, or in other words how well the data cover evenly the full vector measurement range; and secondly, the noise of the measurements. As indicated above, the scalar and vector magnetometers are of very high precision, 20 and 50 pT_{RMS}, respectively. Nevertheless, there are other effects, which contribute to the noise or disturbances and which should be taken into account. However, they will not be treated fully in this paper, although it is worth mentioning them in order to minimize their effects as much as possible.

Time synchronization between the scalar and vector magnetometers should be adequate for the time scale of the variations of the Earth's magnetic field. Usually, this is not difficult to obtain by adjusting the times to within 1 s.

Variations of the temperature in the vector magnetometer should be such that they do not affect the parameters. Otherwise, if a model for the temperature behaviour of the parameters is known, it must be applied. The same should be applied if any time-drift effect is detected.

Non-linearities, which have not been taken into account in the model parametrization, can produce some effects that will show up in the residuals and their distribution, which will increase the scatter and hence the overall variance. However, the parameters are always found to be such that the cost function is minimized in the least-squares sense.

The mechanical stability of the set-up is important for a good result. Angular drift of the sensor with respect to the Earth's magnetic field during a setting is seen in the three components. Nevertheless, the scalar field computed from taking the mean values of the time sequence is believed to be drift-free, even if the standard deviation is increased. Otherwise, a straight line can be fitted in order to model the effect, thereby eliminating it.

Another interesting, but undesired, effect is the presence of a homogeneous magnetic gradient in the volume where the calibration takes place. If the distance between the magnetic centre and the mechanical centre of the rotation is different from zero, then the sensor will describe a sphere whose radius is that distance. In this situation, a magnetic gradient produced by a nearby dipole will disturb the volume in such a way that its effect may be coupled to the parameters in various ways. The offset may be affected, as well as the scale factors. If the gradient has a more complicated structure, the non-orthogonalities may also be influenced.

This method of exposing a tri-axial sensor to $\boldsymbol{B}$ vectors in all directions may be used for the in-flight calibration of space-borne vector magnetometers. In particular, in the cases of Ørsted, CHAMP and SAC-C, which also carry a scalar absolute magnetometer. The vector output may be compared with the output of the scalar magnetometer, but attention should be drawn to the fact that the field will be varying along the orbit. Consequently, the difference between the frequency responses of magnetometers may result in different delays, which may depend on the direction of change of the field. The output of a tri-axial magnetometer in space can be compared with the field computed from a suitable IGRF model when the satellite does not carry an absolute scalar magnetometer, as in the case of the Swedish microsatellite Astrid-2, see Merayo *et al* (1999). It would be a poor alternative to use the IGRF for the scalar calibration in the context of Ørsted, CHAMP and SAC-C since they all carry an absolute scalar magnetometer. Hence, a vector calibration will also provide the instrument parameters. This has the drawback that the dynamics of the spacecraft has to be modelled in order to find the attitude of the magnetometer of the spacecraft, unless there are other devices that can provide that information. Furthermore, if the magnetometer and IGRF scalar fields are compared, a scalar calibration may also be performed. This has been applied successfully to sounding rocket magnetometers.

In order to estimate the influence of these sources, the *a posteriori* covariance matrix will be calculated on the basis of the calibrated and orthonormalized field vector $\boldsymbol{B}$. Synthetic data, which have been contaminated by noise and/or are lacking a proper distribution, will be generated to analyse the effects of noise and an ill-suited distribution.

6.1. The distribution of the data

In order to ensure that the least-squares estimator determines the solution with the highest accuracy, a proper uniform distribution of the data over all directions must be accomplished. In our case, a unit sphere should be covered evenly with points over the whole spherical surface, each of them representing equal areas. The elementary surface for unit radius in spherical coordinates, $\mathrm{d}s = \sin\theta\,\mathrm{d}\theta\,\mathrm{d}\phi$, may indicate how to obtain such a distribution. One scheme, Brauer (1997), may be established by dividing the meridians of the globe by equal polar angles, θ_i, and calculating the number of points, $n_{\phi i}$, which are needed in order to have the same distance between consecutive azimuthal angles, ϕ_{ij}. Furthermore, rotation of the parallels by the angle ϕ_{ri} may be done in order to achieve a more even distribution. This is summarized in the next equations:

$$\theta_i = \frac{i-1}{n_\theta - 1}\pi \qquad i = 1, \ldots, n_\theta$$

$$\theta_{ij} = \frac{j}{n_{\phi i}}2\pi - \phi_{ri} \qquad j = 1, \ldots, n_{\phi i}$$

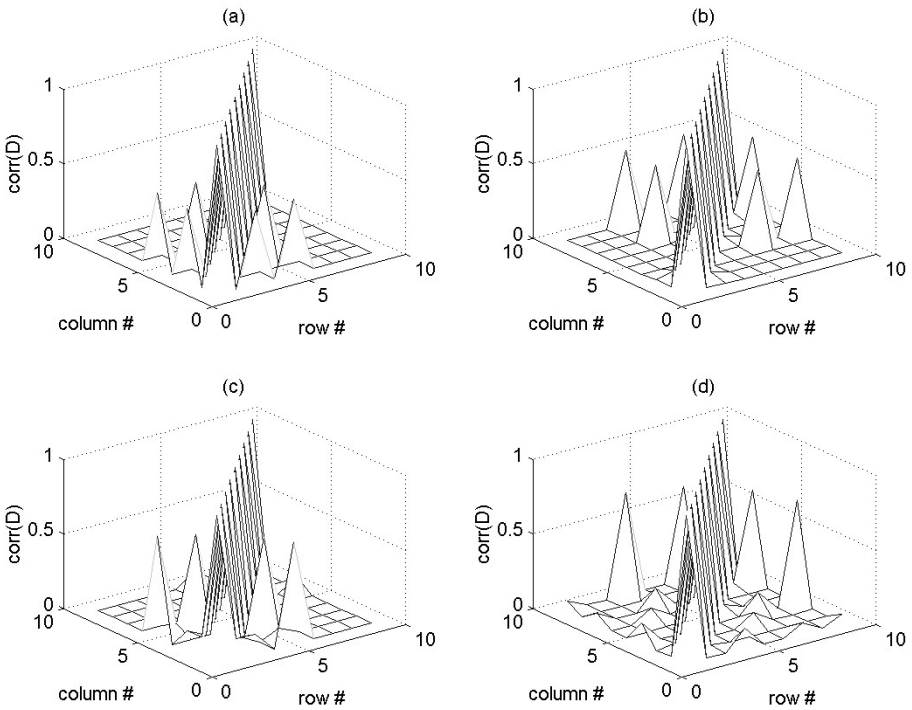

Figure 7. Parameter correlation from an *a posteriori* covariance matrix for evenly (*a*) and slight unevenly (*c*) distributed data from a linear least-squares estimator with a linearized parametrization. For the same data sets (*b*) and (*d*) were obtained by using a non-linear estimator in **A** and $\boldsymbol{O}$. The absolute value of the correlation is shown on the plots. The sum of all off-diagonal elements is 3.00 (*a*), 3.28 (*b*), 3.61 (*c*) and 3.89 (*d*).

$$n_{\phi i} = \text{round}[2(n_\theta + 1)\sin\theta_i + 1]$$

$$\phi_{ri} = \begin{cases} \dfrac{1}{n_{\phi i}}\pi & n_{\phi i} \text{ odd} \\ 0 & \text{otherwise.} \end{cases} \tag{24}$$

Equal-area criteria may be used instead; in that case, if N evenly distributed measurements are to be taken, the number of azimuthal angles in a given parallel at θ_i is modified to be

$$n_{\phi i} = \text{round}\left(\frac{\pi}{2}\frac{N}{n_\theta}\sin\theta_i + 1\right). \tag{25}$$

Alternatively, if equally spaced positions in the θ–ϕ plane are taken for all parallels, the data can be weighted by $\sin\theta$ in (20). The effect of doing this is to have the contributions distributed evenly, generating a good coverage, indirectly.

6.2. The noise

Instrument noise which limits the precision of the data is treated here. The flux-gate magnetometer noise is below 100 pT_{RMS} and therefore the parameters found in the estimation process should have uncertainties which match this precision. If the noise is of the Gaussian type with zero expectation value, it is possible that the mean value of the parameters will be closer to the true value than the standard deviation would indicate. However, if the noise is of some other type then the quality of the estimate of the parameters will be closer to that indicated by the variances.

Table 1. The evolution of the sigma in the kth iteration process for evenly and unevenly distributed data with linear and non-linear estimators: linear L-S fits, (a) and (b); and non-linear L-S fits, (c) and (d); evenly distributed points, (a) and (c); and unevenly distributed points, (b) and (d).

k	0	1	2	3
(a)	2036.116	0.000 274	0.000 0028	0.000 000 26
(b)	2036.116	78.452 014	0.070 4962	0.000 000 05
(c)	2954.611	0.000 274	0.000 0024	0.000 000 22
(d)	2954.611	71.971 104	0.126 4223	0.000 000 05

6.3. A comparison with the non-linear model

A non-linear least-squares model has also been developed for comparison with the linear one. The parametrization is therefore the same as the one expressed in (10) with the matrix **A** given by (11). The usual first approximation of the cost function with gradient corrections to the parameters by the residuals has been implemented in an iterative process. Normalization of the design matrix has been carried out as above.

As expected, the speed of convergence is lower in this case. However, what is surprising is how the *a posteriori* covariance matrix looks compared with the same distribution of the data in the linear case. A data set of evenly distributed data has been generated by making use of (24) with $n_\theta = 8$. This gives a total of 84 points. A second set of data with nine parallels, each of them containing 12 equally spaced azimuthal angular meridians, has also been generated with a total of 108 points, which is slightly unevenly distributed. The actual parameter matrix **A** ($a_{11} = 1.00$, $a_{12} = 0.01$,

Table 2. Variations of the magnetometer parameters produced by contaminating the synthetic data with noise and breaking the even distribution of points on the unit sphere. The standard deviation of each parameter and the standard deviation from the total cost function are also computed.

	Δ $O_{1/2/3}$ nT	Δ $a_{11/22/33}$ 10^{-6}	Δ $a_{12/13/23}$ 10^{-6}	σ $O_{1/2/3}$ nT	σ $a_{11/22/33}$ 10^{-6}	σ $a_{12/13/23}$ 10^{-6}	σ_{rms} nT
Ideal	$<10^{-10}$	$<10^{-10}$	$<10^{-10}$	0.01/ 0.01/ 0.00	0.12/ 0.12/ 0.24	0.24/ 0.24/ 0.24	0.00
X 0.1nT	$<10^{-2}$	0.24/ 0.03/ -0.03	0.01/ -0.38/ 0.11	0.03/ 0.03/ 0.03	0.95/ 0.48/ 0.95	0.95/ 0.95/ 0.95	0.02
X 1nT	0.00/ 0.06/-0.01	0.86/ 1.04/ -0.87	1.29/ 1.17/ 0.84	0.32/ 0.32/ 0.28	8.15/ 7.63/ 8.58	12.87/ 15.26/ 15.26	0.18
Y 1nT	0.00/ 0.01/-0.04	0.04/ 0.23/ -0.15	-1.68/ 1.57/ 0.55	0.28/ 0.28/ 0.25	7.24/ 6.44/ 7.63	11.44/ 12.87/ 12.87	0.16
Z 1nT	-0.04/-0.04/-0.02	-0.20/ 0.29/ 0.69	-0.81/ 0.14/ 0.05	0.27/ 0.28/ 0.24	6.87/ 6.44/ 7.63	11.44/ 12.87/ 12.87	0.15
B 1nT	-0.03/ 0.02/-0.02	-0.74/ -0.25/ 1.26	1.01/ 1.45/ 1.45	0.48/ 0.50/ 0.42	12.22/ 11.44/ 12.87	19.31/ 22.89/ 22.89	0.27
XY1nT	-0.02/ 0.04/ 0.00	1.83/ 0.61/ -1.31	-3.57/ -3.53/ 0.36	0.38/ 0.40/ 0.36	9.79/ 9.66/ 10.86	16.29/ 19.31/ 19.31	0.22
XZ1nT	0.06/ 0.03/ 0.02	0.02/ 0.73/ -0.71	3.16/ -4.67/ 5.59	0.40/ 0.42/ 0.36	10.31/ 9.66/ 11.44	17.17/ 19.31/ 19.31	0.23
YZ1nT	-0.01/-0.06/-0.01	-1.81/ 1.84/ -0.73	0.40/ -3.39/ -1.01	0.38/ 0.40/ 0.34	9.66/ 9.17/ 10.31	16.29/ 18.33/ 18.33	0.22
XYZ 1nT	0.03/ 0.00/-0.03	0.08/ 0.15/ -1.93	3.33/ 5.46/ -1.56	0.48/ 0.50/ 0.42	12.22/ 11.44/ 12.87	19.31/ 22.89/ 22.89	0.27
XYZB 1nT	0.00/-0.09/ 0.13	0.00/ -1.03/ 0.01	1.49/ -0.46/ 4.71	0.71/ 0.75/ 0.64	18.33/ 17.40/ 19.84	30.52/ 34.80/ 34.80	0.41
X 10nT	0.51/-0.16/-0.07	-8.98/ 3.44/ -5.62	-35.83/-16.57/ 19.28	2.47/ 2.60/ 2.22	63.83/ 61.04/ 69.60	105.83/120.68/120.68	1.42
Y 10nT	0.06/ 0.65/-0.15	-3.07/ 11.76/-16.20	8.66/ -3.02/ -2.11	2.89/ 3.04/ 2.60	74.79/ 71.51/ 80.96	123.74/141.10/141.10	1.67
Z 10nT	0.08/-0.31/-0.39	-8.02/ -2.31/ -4.72	9.26/ 27.29/ 35.67	2.93/ 3.06/ 2.61	75.34/ 71.51/ 81.55	123.74/143.03/143.03	1.68
B 10nT	0.29/ 0.51/-0.47	-1.48/ 0.63/ 28.95	-28.43/ 16.31/ 11.26	4.69/ 4.94/ 4.20	120.93/114.79/130.90	199.03/229.10/229.10	2.69
XYZB 0.1nT	0.00/ 0.02/ 0.00	0.16/ -0.26/ -0.01	-0.48/ 0.13/ 0.08	0.06/ 0.06/ 0.06	1.91/ 1.91/ 1.91	2.86/ 3.81/ 3.81	0.04
$\pi/4$ in X	0.02/-0.02/ 0.00	0.51/ -0.15/ -0.37	-0.38/ -0.29/ -0.12	0.06/ 0.06/ 0.05	1.91/ 1.43/ 1.43	2.86/ 2.86/ 2.86	0.03
$\pi/2$ in X	0.08/-0.02/ 0.00	2.25/ 0.83/ -0.38	-1.01/ 0.82/ -0.32	0.06/ 0.06/ 0.06	1.91/ 1.91/ 1.91	2.86/ 3.81/ 3.81	0.04
XYZB 1nT	0.15/-0.05/-0.04	-0.04/ -1.08/ -4.57	-1.15/ 2.29/ -1.13	0.75/ 0.77/ 0.68	19.31/ 18.33/ 20.62	31.36/ 36.66/ 36.66	0.43
$\pi/4$ in X	0.14/-0.02/-0.10	-2.13/ 1.57/ -5.90	7.32/ -8.81/ 0.64	0.75/ 0.65/ 0.56	20.62/ 15.26/ 17.40	28.25/ 34.33/ 30.52	0.38
$\pi/2$ in X	-0.01/-0.20/-0.11	0.44/ -2.64/ 1.56	1.71/ -9.39/ -0.62	0.82/ 0.72/ 0.63	22.89/ 16.74/ 19.31	31.36/ 37.16/ 33.48	0.42
$\pi/2$ in Y	0.14/ 0.22/-0.05	3.48/ 1.62/ 0.94	-3.08/ 5.37/ -1.16	0.50/ 0.53/ 0.45	12.87/ 12.22/ 14.48	21.73/ 24.44/ 24.44	0.29
$\pi/2$ in Z	-0.13/ 0.06/-1.27	-0.79/ -6.83/-36.80	-0.89/ -6.21/ 4.02	0.48/ 0.50/ 0.42	12.22/ 11.44/ 13.05	20.62/ 22.89/ 22.89	0.27

$a_{13} = -0.01$, $a_{22} = 0.95$, $a_{23} = -0.04$ and $a_{13} = 1.10$) and the offset vector $\boldsymbol{O}$ ($O_1 = 5.0$, $O_2 = 1.0$ and $O_3 = -1.0$) used to generate this simulated data set is not important for the result. The sigma or standard deviation in the linear case after the third iteration (table 1) is higher due to machine precision when calculating the squares of the EU_i.

Figure 7 displays the absolute values of the correlations between the parameters calculated from the covariance matrix of two iterative processes. One has been carried out with a linear least-squares estimator for the two data sets (*a*) and (*c*). The same but using a non-linear estimator is depicted in (*b*) and (*d*). It is observed that they are higher for the non-linear case in which the parametrization uses (10*c*) directly, independently of the data distribution. For computing the 'total power' of the sum squared of the off-diagonal terms, there is no doubt that the linear parametrization gives less correlation for estimation of the parameters.

6.4. Simulating non-ideal data

Table 2 has been created by contaminating the evenly distributed synthetic data set. This has been done by introducing Gaussian noise of null expectation of 0.1, 1 and 10 nT amplitude into one or more components of $\boldsymbol{B}$. In other cases, the even-distribution condition has been broken by taking field components with polar angles $\pi/4 < \theta < 3\pi/4$ and $0 < \theta < \pi/2$ and neglecting the rest of the sphere. The results of this are shown in table 2. It can be concluded that even the standard deviation is increased when Gaussian noise is added to the data. However, the parameters are estimated better than their standard deviations would predict. This is seen, for example, in the last row of table 2. In this case noise of a level of 1 nT is added to all components including the intensity of the field (*XYZB*) and data only from the southern hemisphere ($\theta > \pi/2$) have been taken.

The effect of adding noise to the field components influences the parameters very little even if the variance is higher. This occurs for Gaussian noise. As the distribution becomes uneven the errors in the parameters increase as expected.

7. The scalar calibration of a vector magnetometer

During the scalar calibration of a magnetometer, an absolute reference proton magnetometer is operated and therefore the intensity of the field is known at all times. Alternatively, if the experiment is carried out in a magnetic observatory, vector measurements of the field will be available and so the computation of its strength is straightforward. In many cases, both are available, because a combined experiment for calibration and intercalibration with an absolute system is often required.

The vector magnetometer being calibrated is placed on a very stable pillar, which is normally constructed of non-magnetic concrete. Although, it is not necessary to have high mechanical stability, for the reasons explained in section 6; it is wise to start with a firm support. The magnetic sensor is attached to a mechanism like the one in figure 8 and it is rotated in all directions to achieve an even distribution of points following (24). 84 points ($n_\theta = 8$) are sufficient to estimate the magnetometer parameters confidently. For each of these settings, a number of samples equivalent to a few minutes time are acquired and recorded both from the flux-gate vector magnetometer and from the absolute magnetometer. The preparation of the data or pre-processing has to be done before the analysis of the data. Therefore, the engineering outputs and scalar readings have to be averaged and merged and then these averages constitute the inputs for the fitting subroutines.

By applying the algorithm described in section 5 and repeated in (20), the parameter vector $\boldsymbol{p}$ is found. One iteration is enough to estimate $\boldsymbol{p}$ and a second suffices to get rid of the B_0 correction of the absolute field, as

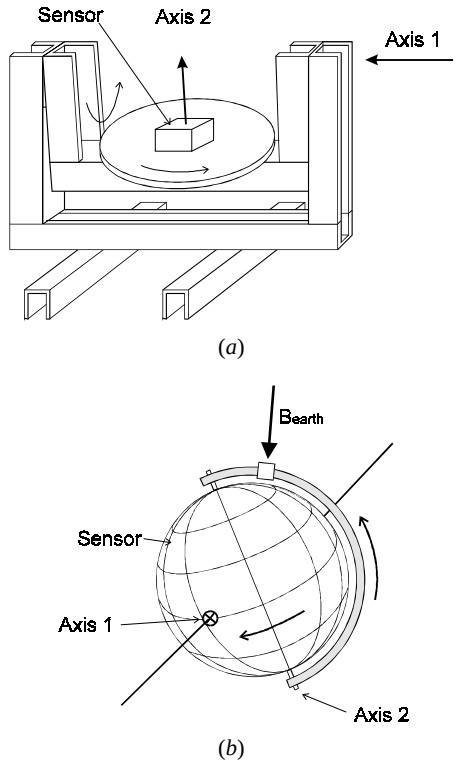

Figure 8. The turntable (*a*) which is used to rotate the sensor in all directions to obtain an even distribution. The magnetic sensor (*b*) is exposed to the magnetic field of the Earth; rotation about two perpendicular axes suffices to get all directions.

discussed. However, a few iterations are performed in order to minimize truncation errors and to ensure that one obtains a good behaviour of the process. A set of data from a *thin shell* (Merayo *et al* 1995) with 151 points, which has been obtained in a coil system, is used in order to compare the coefficients estimated from a usual vector calibration with the scalar calibration coefficients. The strength of the field is about 50 μT. This set belongs to the flight unit of the Ørsted vector magnetometer in the magnetic-coil facility of Magnetsrode, at the Technical University of Braunschweig. In the third iteration, the linear transformation that relates the magnetometer's EU_i to the physical field is found to be

$$\begin{bmatrix} B_1 \\ B_2 \\ B_3 \end{bmatrix}_{IRFS} = \begin{bmatrix} 0.998\,650\,57 & 0.001\,455\,19 & -0.000\,478\,06 \\ 0 & 1.002\,790\,02 & -0.000\,416\,17 \\ 0 & 0 & +1.004\,420\,08 \end{bmatrix} \begin{bmatrix} EU_1 + 14.558 \\ EU_2 - 01.287 \\ EU_3 + 31.138 \end{bmatrix} \text{(nT)}. \tag{26}$$

The uncertainties are calculated on the basis of a doubling of the cost function. These are computed with a marginal error of 5 pT, which is set to be ten times lower than the instrument noise. The standard deviations of **A** and $\boldsymbol{O}$ are

$$\sigma_A = \begin{bmatrix} 5\times10^{-6} & 10\times10^{-6} & 10\times10^{-6} \\ 0 & 6\times10^{-6} & 10\times10^{-6} \\ 0 & 0 & 6\times10^{-6} \end{bmatrix} \left(\frac{\text{nT}}{\text{eu}}\right)$$

$$\sigma_O = \begin{bmatrix} 0.19 \\ 0.21 \\ 0.21 \end{bmatrix} \text{(nT)}. \tag{27}$$

Table 3. A comparison of the standard deviations of the residuals with scalar and vector calibrations for the result of figure 9.

	σ_X (nT)	σ_Y (nT)	σ_Z (nT)	σ_B (nT)
Scalar calibration	0.086	0.478	0.143	0.046
Vector calibration	0.132	0.99	0.116	0.118

It is interesting to compare the residuals using parameters calculated by the scalar calibration procedure with those obtained using vector calibration parameters. In figure 9, these differences are plotted. The top three plots show the residuals between the vector components of the magnetometer and coil system after the coil system has been rotated into the magnetometer system. In the bottom plot, the corresponding residuals for the scalar field, which is the cost function that has been minimized after squaring and summing, are shown. Table 3 compares the individual sigmas for the residuals found in a vector calibration and in a scalar calibration.

The sensitivities and non-orthogonality angles are calculated by using (11*b*) and (7). In order to get an estimate of ξ_3, it is firstly assumed to be unity. Therefore, c_{ij} are computed using (7) and afterwards a closer value of ξ_3 is found from (8). This new value of ξ_3 is used to recalculate the c_{ij}. The parameters are given in table 4.

These angles measure the deviation from 90°, therefore it is more convenient to use the sine function. Since they are very small, they can be approximated by the argument of the sine functions in (7):

$$\nu_{12} \equiv \sin\left((\boldsymbol{w}_1, \boldsymbol{w}_2) - \frac{\pi}{2}\right) \cong -c_{12}$$

$$\nu_{13} \equiv \sin\left(\frac{\pi}{2} - (\boldsymbol{w}_1, \boldsymbol{w}_3)\right) \cong c_{13}$$

$$\nu_{23} \equiv \sin\left(\frac{\pi}{2} - (\boldsymbol{w}_2, \boldsymbol{w}_3)\right) \cong c_{23}. \tag{28}$$

Their statistical values are given in table 5.

Another interesting diagnostic is the plotting of a global map and contour of the points and residual distribution, respectively. Thereby, any systematic angular behaviour of the sensor may be revealed. For the example treated here this is done in figure 10. Contour lines are generated from −1.0 to 1.0 nT with a step of 0.1 nT. From looking at the plot, one could conclude that there is no systematic angular trend, but the residuals are rather randomly distributed.

8. Discussion and conclusion

The intrinsic reference-frame system (IRFS) of the magnetic sensor, which is constructed from the skewed mechanical axes, is proven to be a very precise reference frame for the magnetometer. The pointing accuracy is 2 arcsec, which is equivalent to an error of 10 ppm. Although a few arcminutes of skewness destroys the orthogonality of the sensor, a scalar calibration can resolve the problem and determine the parameters needed to rebuild an orthonormal system.

The data set obtained from a coil system has been used in order to compare the parameters found by the vector and

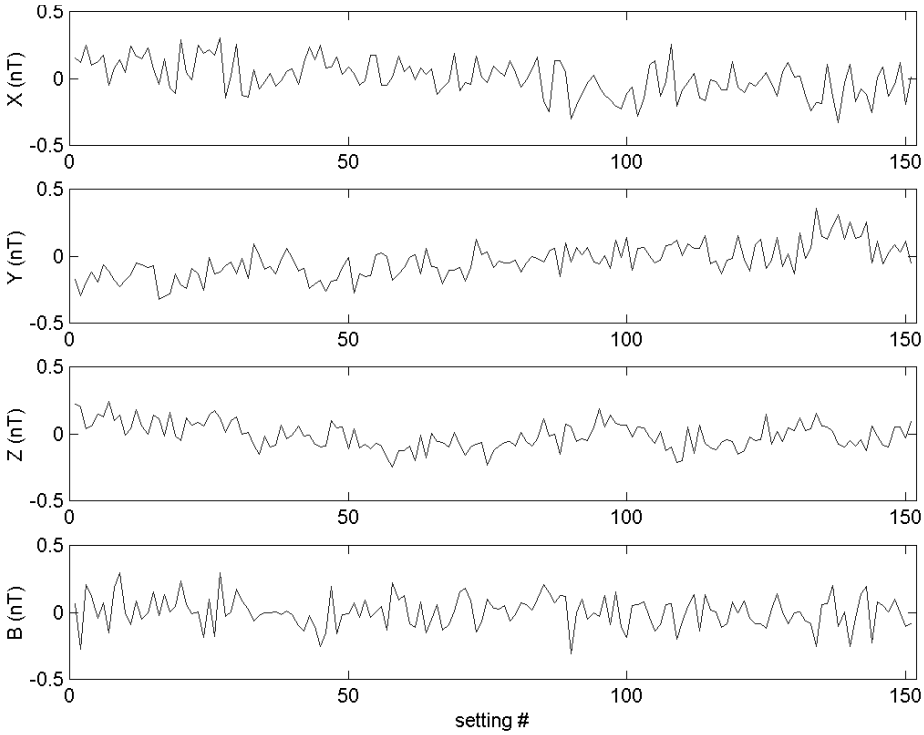

Figure 9. The difference between the vector components and the field intensity of the coil system and of the magnetometer. The calibration parameters of the magnetometer are estimated from the scalar calibration and the coil system is rotated into the magnetometer system.

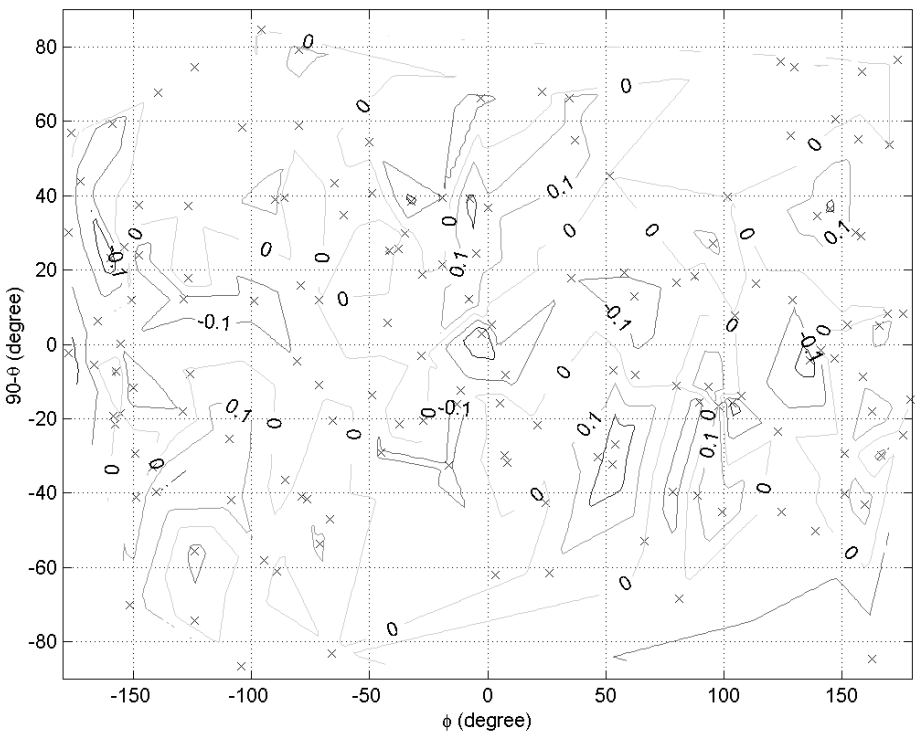

Figure 10. A global map showing the angular distribution of the data-set points on a unit sphere. The 0 nT and other contour lines are plotted in order to detect any systematic angular behaviour. No such effect is seen.

the scalar methods. The sources of errors in this case are several, such as the coil system which has to be calibrated by a proton magnetometer (using, for example, the same method as that described in this paper), and one has to maintain very stable conditions. Nevertheless, the linear scalar method using only the Earth's field proves to be very robust and presents a unique solution for the data set given. The fact that the CSC sensor has an extremely good linear response

Table 4. Parameter values for the data set giving the residuals of figure 9 by using equations (11) and (13). The strength of the residual field B_0 is 34.526 nT.

	1	2	3
s_i	0.998 650 57	1.002 788 96	1.004 419 88
γ_i	−0.001 451 14	1.000 001 05	x
ξ_i	0.000 475 35	0.000 414 33	1.000 000 19
B_0 (nT)	−14.858	1.287	−31.138

Table 5. The mean (μ) and standard deviation (σ) of the angles of deviation from orthogonality.

	ν_{12}	ν_{13}	ν_{23}
μ (arcsec)	−299.3	−98.2	−85.6
σ (arcsec)	2.1	2.1	2.1

and behaviour makes the model almost ideal. The standard deviation of the sensitivities is 5 ppm, which is about 0.5 nT of absolute error in the full range of 65 536 nT. The offset is found with 0.2 nT error, which sets the resolution of the instrument in a calibration sense.

Although the algebra needed to express the physical components as functions of the coefficients γ_1, γ_2, ξ_1, ξ_2 and ξ_3 and the engineering units has been developed, it is emphasized that the matrix $\mathbf{A}$ with six parameters and the offset vector $\boldsymbol{O}$ with three components describe the magnetometer entirely. Furthermore, these coefficients may be computed, as was done in table 4, in order to show the skewness of the mechanical basis with respect to the orthogonal basis. The skewness appears to be less than the machining tolerance and the scale factor errors are less than 0.5%, as expected. The offset is a combination of the magnetometer and coil offsets. In table 4, the values of γ_2 and ξ_3 are almost unity, as was expected; therefore, the approximations in (7), (8) and (11) are valid. If any temperature dependence, ΔT, needs to be included in the model, it will be wise to add one temperature coefficient for each of the nine coefficients already parameterized, thus:

$$\mathbf{A}' = \begin{bmatrix} a_{11} + a_{11}^t \Delta T & a_{12} + a_{12}^t \Delta T & a_{13} + a_{13}^t \Delta T \\ 0 & a_{22} + a_{22}^t \Delta T & a_{23} + a_{13}^t \Delta T \\ 0 & 0 & a_{33} + a_{33}^t \Delta T \end{bmatrix}$$

$$\boldsymbol{O}' = \begin{bmatrix} O_1 + O_1^t \Delta T \\ O_2 + O_2^t \Delta T \\ O_3 + O_3^t \Delta T \end{bmatrix}. \qquad (29)$$

Other non-linear behaviours may be modelled as small effects after a scalar calibration has been performed. They can be estimated from a non-linear least-squares iterative method. This will not impose very much constraint on the convergence, since the linear coefficients are very close to the true ones.

The computation of the *a posteriori* covariance matrix gives the smallest correlation for the linearized model. This means that the parameters are found more independently. It tells us as well that the parametrization functions are more orthogonal than those in the non-linear case. This is a well-behaved model and the fact that it is linear (and therefore converges faster) proves that it is superior to the non-linear model.

However, in the scalar calibration the noise is increased. A quantity with null expectation loses this property when it is squared. This can be observed in table 3, in which the comparison with the vector calibration is shown. The effect is propagated through the engineering quantities of the magnetometer; therefore, the expected error of the parameters is set by the noise of the instrument.

The modes of operation of the compact spherical coil (CSC) sensor that has been used for Ørsted and the compact detector coil (CDC) sensor in Astrid-2 are different. When the definition of the reference system is in accordance with the one presented in section 3, it yields an upper-diagonal matrix for the CSC and it will produce a lower-diagonal matrix for the CDC. The full explanation of this situation is beyond the scope of this paper and its clarification will be addressed in a forthcoming paper.

Acknowledgments

Professor Hermann Lühr of the GFZ-Potsdam and Professor Torben Risbo of the University of Copenhagen are thanked for taking part in discussions about some matters in this paper.

References

Backus G E 1970 Non-uniqueness of the external geomagnetic field determined by surface intensity measurements *J. Geophys. Res.* **75** 6337–41

Brauer P 1997 The ringcore fluxgate sensor *PhD Thesis* DTU

Brauer P, Merayo J M G, Nielsen O V, Primdahl F and Petersen J R 1997 Transverse field effect in fluxgate sensors *Sensors Actuators* A **59** 70–4

Brauer P, Risbo T, Merayo J M G and Nielsen O V 2000 Fluxgate sensor for the vector magnetometer onboard the 'Astrid-2' satellite *Sensors Actuators* A at press

Langel R A 1994 Suggested procedures for in-flight calibration of the Ørsted vector magnetometer *Draft proposal, 7 November 1994*

Merayo J M G, Jørgensen P S, Risbo T, Brauer P and Primdahl F 1999 Modelling the Earth's main magnetic field by the spinning Astrid-2 satellite Eos Trans. AGU 80(17) Fall Meet. Suppl. F892 1999

Merayo J M G, Risbo T, Primdahl F, Nielsen O V and Petersen J R 1995 Calibration of the fluxgate CSC vector magnetometers 'Flight' model and 'Flight Spare' model for the Ørsted satellite *Ørsted Satellite Project, technical note* 278

Neubert T 1995 CSC-OVH in-flight calibration *Ørsted technical note* TN-264

Nielsen O V, Brauer P, Primdahl F, Risbo T, Jørgensen J L, Boe C, Deyerler M and Bauereisen S 1997 A high-precision triaxial fluxgate sensor for space applications: layout and choice of materials *Sensors Actuators* A **59** 168–76

Nielsen O V, Petersen J R, Primdahl F, Brauer P, Hernando B, Fernández A, Merayo J M G and Ripka P 1995 Development, construction and analysis of the 'Ørsted' fluxgate magnetometer *Meas. Sci. Technol.* **6** 1099–15

Primdahl F 1986 Instrumentos Geomagnéticos *Publicações do Observatório Nacional do Brasil* 09

Primdahl F, Brauer P, Merayo J M G, Petersen J R and Risbo T 1999 Determining the direction of a geometrical/optical reference axis in the coordinate system of a tri-axial magnetic sensor *Workshop on Calibration of Space-Borne Magnetometers, Institute of Geophysics and Meteorology, Technical University of Braunschweig, 9 March 1999* submitted for publication in *ESA-SP*

Primdahl F and Jensen P A 1982 Compact spherical coil for fluxgate magnetometer vector feedback *J. Phys. E: Sci. Instrum.* **15** 221–6